

COSMOGLOBE DR1. III. First full-sky model of polarized synchrotron emission from all WMAP and Planck LFI data

D. J. Watts^{1*}, U. Fuskeland¹, R. Aurlien¹, A. Basurov¹, L. Bianchi², M. Brilenkov¹, H. K. Eriksen¹, K. S. F. Fornazier³, M. Galloway¹, E. Gjerløw¹, B. Hensley⁴, L. T. Hergt⁵, D. Herman¹, H. Ihle¹, K. Lee¹, J. G. S. Lunde¹, S. K. Nerval^{6,7}, M. San¹, N. O. Stutzer¹, H. Thommesen¹, and I. K. Wehus¹

¹ Institute of Theoretical Astrophysics, University of Oslo, Blindern, Oslo, Norway

² Dipartimento di Fisica, Università degli Studi di Milano, Via Celoria, 16, Milano, Italy

³ Instituto de Física, Universidade de São Paulo - C.P. 66318, CEP: 05315-970, São Paulo, Brazil

⁴ Jet Propulsion Laboratory, California Institute of Technology, 4800 Oak Grove Drive, Pasadena, California, U.S.A.

⁵ Department of Physics and Astronomy, University of British Columbia, 6224 Agricultural Road, Vancouver BC, V6T1Z1, Canada

⁶ David A. Dunlap Department of Astronomy & Astrophysics, University of Toronto, 50 St. George Street, Toronto, ON M5S 3H4, Canada

⁷ Dunlap Institute for Astronomy & Astrophysics, University of Toronto, 50 St. George Street, Toronto, ON M5S 3H4, Canada

October 17, 2023

ABSTRACT

We present the first model of full-sky polarized synchrotron emission that is derived from all *WMAP* and *Planck* LFI frequency maps. The basis of this analysis is the set of end-to-end reprocessed COSMOGLOBE Data Release 1 sky maps presented in a companion paper, which have significantly lower instrumental systematics than the legacy products from each experiment. We find that the resulting polarized synchrotron amplitude map has an average noise rms of $3.2 \mu\text{K}$ at 30 GHz and 2° FWHM; 30 % lower than the recently released BEYONDPLANCK model that included only LFI+*WMAP* $Ka-V$ data; and 29 % lower than the raw *WMAP* K -band sensitivity. The mean EE/BB power spectrum ratio is 0.46 ± 0.03 , with amplitudes consistent with those measured previously by *Planck* and QUIJOTE. Assuming a power law model for the synchrotron spectral energy distribution, and using the T-T plot method, we find a full-sky inverse noise-variance weighted mean of $\beta_s = -3.07 \pm 0.07$ between COSMOGLOBE DR1 K -band and 30 GHz, in good agreement with previous estimates. In summary, the novel COSMOGLOBE DR1 synchrotron model is both more sensitive and systematically cleaner than similar previous models, and it has a more complete error description that is defined by a set of Monte Carlo posterior samples. We believe that these products are preferable for all synchrotron-related scientific applications than previous products compared to previous *Planck* and *WMAP* products, including simulation, forecasting and component separation.

Key words. ISM: general – Cosmology: observations, polarization, cosmic microwave background, diffuse radiation – Galaxy: general

Contents

1	Introduction
2	Data products
2.1	<i>WMAP</i> and <i>Planck</i> legacy products
2.2	COSMOGLOBE products
3	Polarized synchrotron amplitude
3.1	Polarized amplitude maps
3.2	Comparison with independent datasets
3.3	Power spectra
4	Polarized synchrotron spectral indices
4.1	T-T plot analysis
4.1.1	Method
4.1.2	Results
4.2	Parametric component estimation
5	Discussion and conclusion
A	T-T Plots

1 Understanding the polarization of the cosmic microwave background (CMB) is a primary focus of observational cosmology
2 in the coming decades. Following the success of the satellite-based *COBE* (Smoot et al. 1992; Mather et al. 1994; Hauser et al. 1998), *Wilkinson Microwave Anisotropy Probe* (*WMAP*) (Bennett et al. 2013), and *Planck* (Planck Collaboration I 2020) experiments, as well as sub-orbital experiments including BICEP4 (Ade et al. 2021), ACT (Madhavacheril et al. 2023), CLASS (Eimer et al. 2023), SPIDER (SPIDER Collaboration et al. 2022), and many others, the future *LiteBIRD* satellite (LiteBIRD Collaboration et al. 2023) and ground-based Simons Observatory (Ade et al. 2019) and CMB-S4 (Abazajian et al. 2019) experiments will create the most sensitive maps of the polarized sky yet, providing the most stringent constraints on primordial gravitational waves.
3 In the past decade, uncertainties on cosmological constraints have been limited not only by instrumental sensitivity, but by incomplete knowledge of the sky itself. Uncertainty in the sky model has been mitigated by designing experiments with broad frequency coverage, such as *WMAP* (Bennett et al. 2013) and *Planck* (Planck Collaboration I 2020), or analyzing maps from
4
5
6
7
8
9
10
11
12
13

* Corresponding author: D. Watts; duncanwa@astro.uio.no

different experiments jointly (e.g., [Bennett et al. 1996](#), [Bennett et al. 2013](#), [Planck Collaboration X 2016](#), and [BICEP2/Keck Array and Planck Collaborations 2015](#), among many others). A major impediment to joint analyses is the difficulty of combining data with different survey strategies and incompletely characterized systematics. In order to maximize scientific throughput, one must either design an experiment that can characterize every relevant observable on its own, or jointly analyze different datasets in the same joint framework.

The BEYONDPLANCK project achieved such joint analysis by combining external data, specifically, the Haslam 408 MHz map ([Haslam et al. 1982](#)), *WMAP* *Ka*–*V* bands, *Planck* 353 GHz in polarization, and *Planck* 857 GHz in intensity, while analyzing the *Planck* 30, 44, and 70 GHz time-ordered data (TOD) ([BEYONDPLANCK Collaboration 2023](#)). The *Planck* LFI experiment showed that raw detector sensitivity was not enough to obtain high-fidelity sky maps; [Planck Collaboration II \(2020\)](#) found that the detector gain solution depended on the assumed polarization and intensity of the sky. To break this circular dependency, the BEYONDPLANCK framework solved for the intrinsic sky signal and instrumental parameters iteratively, providing an accurate model of the entire system with full error propagation. By leveraging the external *WMAP*, Haslam, and *Planck* HFI data, BEYONDPLANCK was able to create *Planck* LFI maps of cosmological quality at all frequency channels, while generating a robust model of the foreground sky.

The COSMOGLOBE project¹ has generalized the BEYONDPLANCK analysis by additionally processing *WMAP* *K*–*W*-band TOD jointly with *Planck* LFI TOD. This framework, fully described in [Watts et al. \(2023b\)](#) and [Watts et al. \(2023a\)](#), not only improved the quality of the *WMAP* maps themselves, but provided the most robust full-sky model of low frequency polarized emission available to date. In particular, poorly-measured modes due to transmission imbalance ([Jarosik et al. 2007](#)) have been effectively marginalized over, in large part due to the use of a global sky model that was not used in the fiducial *WMAP* analyses. The removal of poorly measured modes alone will improve Galactic modelling for years to come, as the current state-of-the-art models use *WMAP* *K*-band (23 GHz) maps as polarized synchrotron templates for modeling of synchrotron without any mitigation of the poorly-measured modes ([Delabrouille et al. 2013](#); [Thorne et al. 2017](#); [Zonca et al. 2021](#)).

In order to make use of the synchrotron model, we require robust estimates of the spectral behavior. Fundamental properties of synchrotron, such as the spectral index as a function of frequency, spatial decorrelation, and even the functional form of the spectral energy distribution (SED), are yet to be fully characterized observationally. Modern attempts have been frustrated by the lack of high signal-to-noise data; [de Belsunce et al. \(2022\)](#), for example, find spectral indices ranging from -5 to -1 , discrepant with predictions from direct measurements of the cosmic ray energy spectrum of 2–3 ([Rybicki & Lightman 1985](#); [Orlando & Strong 2013](#); [Neronov et al. 2017](#)), largely due to fitting too many parameters to data with too low signal-to-noise ratio. Such analyses can be greatly improved by combining complementary data sets.

While the combination of as many datasets as possible would help to constrain polarized synchrotron's large-scale properties, long-standing discrepancies between existing datasets complicate this. As shown by, for example, [Planck Collaboration X \(2016\)](#) and [Weiland et al. \(2018\)](#), there are discrepancies in the polarization measurements of *WMAP* and *Planck*, partially due

known instrumental effects ([Bennett et al. 2013](#); [Planck Collaboration II 2020](#)). [BeyondPlanck Collaboration \(2023\)](#) largely resolved these issues for LFI, while [Watts et al. \(2023b\)](#) removed the poorly measured modes in *WMAP*. In the first COSMOGLOBE data release, of which this paper is a part, [Watts et al. \(2023a\)](#) demonstrated that the polarized maps resulting from these two experiments are consistent at the noise level after recalibrating both experiments jointly. At the same time, the new maps must be validated by a variety of analysis methods. As noted in, for example, [Weiland et al. \(2022\)](#), simply using a different analysis pipeline can result in different estimations of the underlying frequency map. As such, we take care to appropriately marginalize over instrumental effects in our spectral analysis, and attempt to find the physical reason for the differences between different pipelines.

With these longstanding discrepancies addressed, the main goal of the current paper is to derive the highest signal-to-noise ratio model of polarized synchrotron emission from *Planck* and *WMAP* data published to date, including both amplitude and spectral index parameters. This work is organized as follows. In Sect. 2, we provide a brief overview of the data products and the COSMOGLOBE data processing. Section 3 discusses the polarized amplitude of the COSMOGLOBE synchrotron model, its overall uncertainty, and the power spectrum properties compared to external products. Section 4 estimates the synchrotron spectral index using both the T-T plot method and Gibbs sampling using Commander, followed by discussions and conclusions in Sect. 5.

2. Data products

The data products used in this paper are the *WMAP* and *Planck* LFI maps, with most of the statistical weight coming from 23–33 GHz, or the *WMAP* *K* and *Ka* bands and LFI's 30 GHz band. These frequencies are low enough that we can treat them as synchrotron tracers and hence ignore thermal dust and CMB emission, but not so low that we need to take into account effects like Faraday rotation, such as in S-PASS data ([Krachmalnicoff et al. 2018](#); [Fuskeland et al. 2021](#)). We describe the legacy data products and the data products from the COSMOGLOBE *WMAP* reanalysis in the following subsections.

2.1. WMAP and Planck legacy products

WMAP was a NASA-funded satellite mission that observed from August 2001 to August 2010, designed to characterize the microwave sky well enough to measure the primary CMB anisotropies across the full sky down to a resolution of 13' FWHM. Using a differential scanning strategy inspired by COBE/DMR, *WMAP* produced maps of the sky at 23 (*K*), 33 (*Ka*), 41 (*Q*), 61 (*V*), and 94 GHz (*W*) in both polarization and total intensity ([Bennett et al. 2013](#)), with angular resolutions of 53' at 23 GHz to 13' at 94 GHz. The maps are available on the LAMBDA website.²

The *Planck* Low Frequency Instrument (LFI) produced 30, 44, and 70 GHz maps in both intensity and polarization, while the High Frequency Instrument (HFI) produced 100, 143, 217, 353 GHz maps in polarization and intensity, and 545 and 857 GHz maps in intensity alone. The LFI data have somewhat lower white noise and higher angular resolutions (of 30', 20', and 13' FWHM for 30, 44, and 70 GHz) than *WMAP*. In contrast to *WMAP*, the LFI measurements used a single horn,

¹ cosmoglobe.uio.no

² https://lambda.gsfc.nasa.gov/product/wmap/dr5/m_products.html



Fig. 1. Polarized intensity and white noise levels of (top): WMAP K -band, (middle): Planck 30 GHz, and (bottom): synchrotron amplitude from the COSMOGLOBE Gibbs chain, all evaluated at 30 GHz with a resolution of $72'$. The leftmost column is a 10° width square centered a low signal-to-noise regions highlighted by a red square in the top middle column's panels, the middle column shows the polarized total amplitude, P , and the rightmost column shows the rms noise for the frequency maps and the posterior standard deviation of the synchrotron amplitude.

and the *Planck* scanning strategy followed rings closely aligned with ecliptic meridians. The *Planck* legacy datasets, PR3 ([Planck Collaboration I 2020](#)) and PR4 ([Planck Collaboration Int. LVII 2020](#)), are both publicly available on the *Planck* Legacy Archive (PLA).³

2.2. COSMOGLOBE products

A main goal of COSMOGLOBE is to perform joint end-to-end analyses on multiple data sets, preferably beginning from raw TOD. An important advantage of such end-to-end processing is that it offers a robust path to breaking internal degeneracies within and between different data sets, thereby in general reducing the magnitude of systematic effects. The analysis described by [BeyondPlanck Collaboration \(2023\)](#) and [Watts et al. \(2023a\)](#) were performed on raw TOD, producing cosmological parameters using the Bayesian Gibbs sampler, Commander3 ([Galloway et al. 2023](#)).

In this framework, we produce a full sky model and set of instrumental parameters for each Gibbs sample, and the set of all such samples allows for a thorough characterization of the dependence of low-level instrumental parameters on the sky model. The sky model includes all relevant components in *WMAP* and LFI's frequency range, specifically the CMB, synchrotron, ther-

mal dust, free-free emission, anomalous microwave emission, and radio point sources, the first three of which we model as polarized in our sky model. The full products from this analysis and individual maps are available on the COSMOGLOBE website.⁴

As described by [Watts et al. \(2023a\)](#), COSMOGLOBE DR1 includes 500 end-to-end Gibbs samples, and we perform our basic analysis on each of these samples individually, and then form posterior summary statistics from the full ensemble. This allows us to fully marginalize over the low-level systematic parameters, quantifying the extent to which instrumental propagates to the synchrotron spectral index determination.

3. Polarized synchrotron amplitude

In this section, we give an overview of the polarized synchrotron amplitude properties. In Sec. 3.1, we focus on the map-based properties, and compare with independently processed results in Sec. . In Sec. 3.3, we evaluate the power spectrum of the polarized synchrotron map and compute the B-to-E ratio.

⁴ <https://www.cosmoglobe.uio.no/products/cosmoglobe-dr1.html>

³ <https://pla.esac.esa.int/>

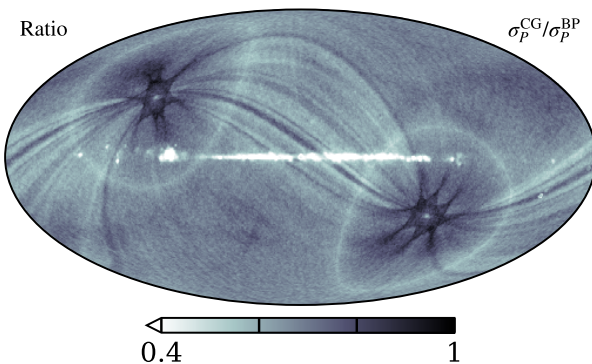


Fig. 2. COSMOGLOBE posterior standard deviation divided by BEYONDPLANCK posterior standard deviation.

3.1. Polarized amplitude maps

When using external data for polarized foreground cleaning, the choices for high signal-to-noise full sky constraints are either *WMAP* *K*-band, *Planck* LFI 30 GHz, or models derived from combinations of these data, as in COSMOGLOBE. From the perspective of pure statistical uncertainty, a combination of multiple independent datasets would yield component maps that are more sensitive than each individual component. However, unmodeled systematic uncertainties in the underlying datasets, left untreated, can induce map effects that can leak into astrophysics and cosmological constraints. As shown in Watts et al. (2023a), a single sky model that all datasets are calibrated against improves the low-level instrumental processing, and allowing for degeneracies, such as transmission imbalance uncertainty in *WMAP* and differential gain uncertainty in LFI, to be broken. Within the COSMOGLOBE DR1 framework, the polarization maps from *WMAP* and *Planck* LFI are consistent with each other at the $10\,\mu\text{K}$ level, consistent with the instrumental white noise of the datasets.

The COSMOGLOBE DR1 frequency maps are free from previously reported systematics, and are consistent between different frequencies and instruments. Therefore, a coherent model of polarized synchrotron emission can be made by combining the *WMAP* and LFI frequency maps. The polarized spectral amplitude determined from COSMOGLOBE fully utilizes the *Planck* and *WMAP* joint reprocessed data, as shown in Fig. 1. We plot the total polarized amplitude $P = \sqrt{Q^2 + U^2}$ for ease of comparison. The visible noise bias from plotting this positive definite quantity highlights the reduction in the noise level in the COSMOGLOBE synchrotron map as compared to the *K*-band and 30 GHz maps. This is especially relevant in the leftmost column of Fig. 1, an inset of a high Galactic latitude, low signal region.

The *WMAP* *K*-band data and LFI 30 GHz data, as the highest signal-to-noise full-sky polarized maps of Galactic synchrotron emission, are the main contributors to our knowledge of the polarized amplitude. The slightly higher angular resolution 30 GHz map has lower signal-to-noise than the *K*-band data, but by combining the multi-resolution maps we are able to produce a clean map of the synchrotron emission evaluated at 30 GHz with a FWHM of 1° .

BEYONDPLANCK and COSMOGLOBE data products are both created using the Commander3 pipeline, but COSMOGLOBE benefits from using the *K*-band data. Therefore, the synchrotron map from BEYONDPLANCK (BeyondPlanck Collaboration 2023) has lower resolution and higher noise; the COSMOGLOBE synchrotron

map has a mean posterior rms of $3.4\,\mu\text{K}$, nearly a factor of two improvement over the BEYONDPLANCK map. Much of the improvement can be seen when taking the ratio of the posterior rms maps, as in Fig. 2. As expected, the regions with the lowest ratios correspond to the deep *WMAP* observations and the Galactic plane, which benefit from the high signal-to-noise of the *K*-band data. Regions with nearly identical rms include regions with the highest *Planck* depth, such as the ecliptic poles, and regions less deeply observed by *WMAP*, corresponding to planet crossings and artifacts from the processing mask. Notably, stripes corresponding to the *Planck* scan strategy also show improvement with respect to BEYONDPLANCK. This is due to the interaction between the sky model and LFI's instrumental parameters – with the high signal-to-noise *K*-band data, the sky model becomes more stable, and LFI's relative gain solution becomes better determined.

To quantify the noise improvement in the synchrotron maps over pure templates based on either *K*-band or 30 GHz maps, we compare the posterior standard deviation of the COSMOGLOBE synchrotron map with the frequency maps' rms values. The posterior standard deviation maps are $\lesssim 1\,\mu\text{K}$ for *K*-band, while temperature-to-polarization uncertainty in 30 GHz contributes at the $2\,\mu\text{K}$ level (see, e.g., Watts et al. 2023a and Basyyrov et al. 2023 for further details). An informative prior of $D_\ell = 200e^{-\ell(\ell+1)\sigma^2}\,\mu\text{K}^2$, where σ is the Gaussian width corresponding to a FWHM of $30'$, is applied during polarized synchrotron amplitude fitting, essentially downweighting low signal-to-noise fluctuations at angular scales $\lesssim 30'$, or $\ell \gtrsim 360$ (Svalheim et al. 2023a). Therefore, the rms noise contributions are relevant at roughly $N_{\text{side}} = 128$. To compare the COSMOGLOBE white noise level with the *K*-band and 30 GHz white noise levels, we simulate realizations of the expected white noise smoothed to $72'$ and scale the maps to 30 GHz assuming $\beta_s = -3.1$, consistent with the post-processed synchrotron map. We display these smoothed rms maps in the right column of Fig. 1.

At these resolutions, the mean rms for *K*-band and 30 GHz are $4.8\,\mu\text{K}$ and $4.7\,\mu\text{K}$ respectively, compared to the mean value of $3.4\,\mu\text{K}$ for the COSMOGLOBE DR1 synchrotron map; this is consistent with adding the scaled maps in quadrature. While this may seem obvious on its face, the combination of *WMAP* *K*-band and *Planck* 30 GHz is not straightforward due to instrumental effects that remain in the maps, notably poorly measured modes in *WMAP* (Bennett et al. 2013; Weiland et al. 2018) and gain uncertainty in *Planck* (*Planck* Collaboration II 2020). These effects remain in the official *WMAP9* (Bennett et al. 2013) and *Planck* PR3/PR4 (*Planck* Collaboration II 2020; *Planck* Collaboration Int. LVII 2020) maps, making combination of these datasets non-ideal for Galactic science and cosmological analyses. However, the end-to-end BEYONDPLANCK (BeyondPlanck Collaboration 2023) products effectively removed the gain uncertainty modes from the *Planck* LFI maps, and the COSMOGLOBE DR1 results (Watts et al. 2023a) are free from the poorly measured modes. As shown in Fig. 46 of Watts et al. (2023a), the *Planck* 30 GHz and the *WMAP* *K*-band are consistent with each other at the $10\,\mu\text{K}$ level, indicating that the maps are consistent with each other down to the white noise level.

This polarized synchrotron map, derived from consistent datasets, has a white noise level 29 % lower than both the *K*-band map and the 30 GHz map, with minimal systematic uncertainties in the posterior standard deviation. Therefore, the synchrotron map derived from the COSMOGLOBE DR1 Gibbs chain should be used for the characterization and removal of polarized synchrotron emission between 23–90 GHz.

3.2. Comparison with independent datasets

As a check on the polarized synchrotron amplitude, we compare the COSMOGLOBE polarized synchrotron map with the frequency maps produced in the main DR1 chain, paying special attention to maps with the highest polarized synchrotron signal-to-noise ratio; K , Ka , 30 GHz, and 44 GHz. These maps should agree by virtue of being produced in the same analysis framework. We compare with the *WMAP9* and PR3 maps. Of these, the *WMAP9* results can be considered the most independent, as the results were produced with no sky model assumptions, and were produced before the *Planck* polarized maps were publicly available, thus making the analysis completely unbiased. The PR3 maps should also be independent of the *WMAP9* results, although the *WMAP9* results were available during PR3 production, so this analysis cannot be truly considered blinded to existing *WMAP* data. The PR4 analysis was performed using both the LFI and HFI dataset in a joint processing framework, conceptually similar to the framework in COSMOGLOBE DR1. Since we are highlighting the differences between joint processing and independent processing frameworks, we leave out PR4 in this specific comparison.

Using the polarized synchrotron model generated in the main COSMOGLOBE DR1 chain, we can evaluate the synchrotron emission at each frequency and compare it with the maps produced by various different processing pipelines. We evaluate the COSMOGLOBE sky model using the `cosmoglobe` Python package to evaluate the sky model using the full bandpass information of each instrument.⁵ Visual inspection of the data with the sky model subtracted and smoothed to a common 5° Gaussian beam provides a robust check on the quality of the model and the underlying data.

The first and third rows of Fig. 3 show the *WMAP9* and PR3 residuals with respect to the COSMOGLOBE sky model in second and fourth rows. These residuals match previously-documented observational effects in both experiments. In particular, the *WMAP* maps show artifacts of the poorly-measured modes due to transmission imbalance in the differential horns (Jarosik et al. 2007; Bennett et al. 2013), while the PR3 differences are mostly due to relative gain errors (Planck Collaboration II 2020; Planck Collaboration Int. LVII 2020). In contrast, the synchrotron model matches the COSMOGLOBE DR1 frequency maps within $5\mu\text{K}$ across the sky, with few observational artifacts.

Most of the residuals are associated with the Galactic plane and diffuse structures uncorrelated with the *WMAP* and *Planck* observation strategies. The positive excess in the Ka Stokes Q map could be due to unmitigated data processing artifacts. While a similar large-scale excess can also be seen in the LFI 30 and 44 GHz Stokes Q maps, the signature strongly resembles the bandpass correction in *WMAP* K -band, suggesting incomplete treatment of bandpasses could be contributing to this large-scale signal. The LFI residuals, while much improved, still show trace residuals, especially near the Galactic center, that are somewhat correlated with the gain correction templates, but not at a level that high Galactic latitude features can be identified.

As the scale of instrumental residuals have been reduced to below the white noise level for each of the synchrotron-dominated full-sky polarization maps, we are now able to associate the residuals with potential modifications to the sky model. Specifically, the COSMOGLOBE DR1 processing sampled a spatially constant β_s with a final mean of $\beta_s = -3.15$. In Sec. 4,

we analyze these maps allowing for spatial dependence in the polarized synchrotron spectral index to determine the extent to which true on-sky variation can be determined based on these maps.

3.3. Power spectra

Due to the importance of foreground removal for precise primordial gravitational wave measurement, the ratio of synchrotron B-modes to E-modes has long been studied, and has been consistently noted to be less than one (Page et al. 2007; Planck Collaboration X 2016; Planck Collaboration IV 2018; Krachmalnicoff et al. 2018; Rubiño-Martín et al. 2023; Eimer et al. 2023). The physical mechanism for this has been discussed in the context of Galactic magnetic fields and polarized thermal dust (e.g., Kandé et al. 2017, ?, Vacher et al. 2023), but similar mechanisms are likely to be in play for synchrotron polarization.

To estimate the power spectra without a noise bias, we performed a `Commander3` run using half-mission splits with odd-numbered scans and even-numbered scans being analyzed in runs labeled HM1 and HM2, analogous to the *Planck* “half-mission” splits. Each of these chains were performed using the same data as in the main COSMOGLOBE chain, with 200 samples each.⁶ The highest quality of similar half-mission splits that are publicly available are from the *Planck* PR3 analysis, as discussed in Planck Collaboration IV (2018). We therefore compute power spectra from the PR3 results and compare them directly with the COSMOGLOBE HM splits.

We performed power spectrum estimation using `NaMaster` (Alonso et al. 2019) with the *Planck* 2018 common polarization mask with $f_{\text{sky}} = 0.78$ and 1° apodization. To quantify the uncertainty, we take the cross spectrum for each pair of Gibbs samples from HM1 and HM2 respectively, and report the 68 % confidence intervals on this posterior. The power spectra are displayed in Fig. 4, and the standard deviation is computed using the within-bin variance of each bin, with the posterior standard deviation of the Gibbs chain added in quadrature for the COSMOGLOBE spectra. Other than the very lowest and very highest multipole bins, there is good per-multipole agreement between both the PR3 and COSMOGLOBE DR1 spectra. For comparison, we plot the E-mode power spectrum predicted by the *Planck* 2018 cosmological parameters.

Following Planck Collaboration IV (2018), we perform power law fits to the power spectra of the form $\mathcal{D}_\ell^{\text{EE}/\text{BB}} = A_s^{\text{EE}/\text{BB}}(\ell/80)^\alpha$, using multipoles $\ell \in [2, 140]$. The 68 % confidence intervals for each quantity, including the $A_s^{\text{BB}}/A_s^{\text{EE}}$ ratio, are reported in Table 1. The primary differences between the fits to the two datasets are $\sim 2\sigma$ discrepancies in the A_s^{BB} and α_s^{EE} fits, while all others are consistent within $\simeq 0.5\sigma$. The primary drivers of these differences are lower $\mathcal{D}_\ell^{\text{BB}}$ and higher $\mathcal{D}_\ell^{\text{EE}}$ in the lowest bins. These fit parameters yield a value of $A_s^{\text{BB}}/A_s^{\text{EE}}$ of 0.40 for the COSMOGLOBE splits and 0.46 for PR3. The ratio we determined for the PR3 split is lower than the reported value of 0.34 in Planck Collaboration IV (2018), using a nearly identical methodology. Despite the discrepancies between the values in this paper and Planck Collaboration IV (2018), it is clear that the COSMOGLOBE DR1 ratio is lower than that of *Planck* PR3.

⁵ <https://cosmoglobe.readthedocs.io/en/latest/tutorials/skymodel.html>

⁶ These products can be found at cosmoglobe.uio.no.

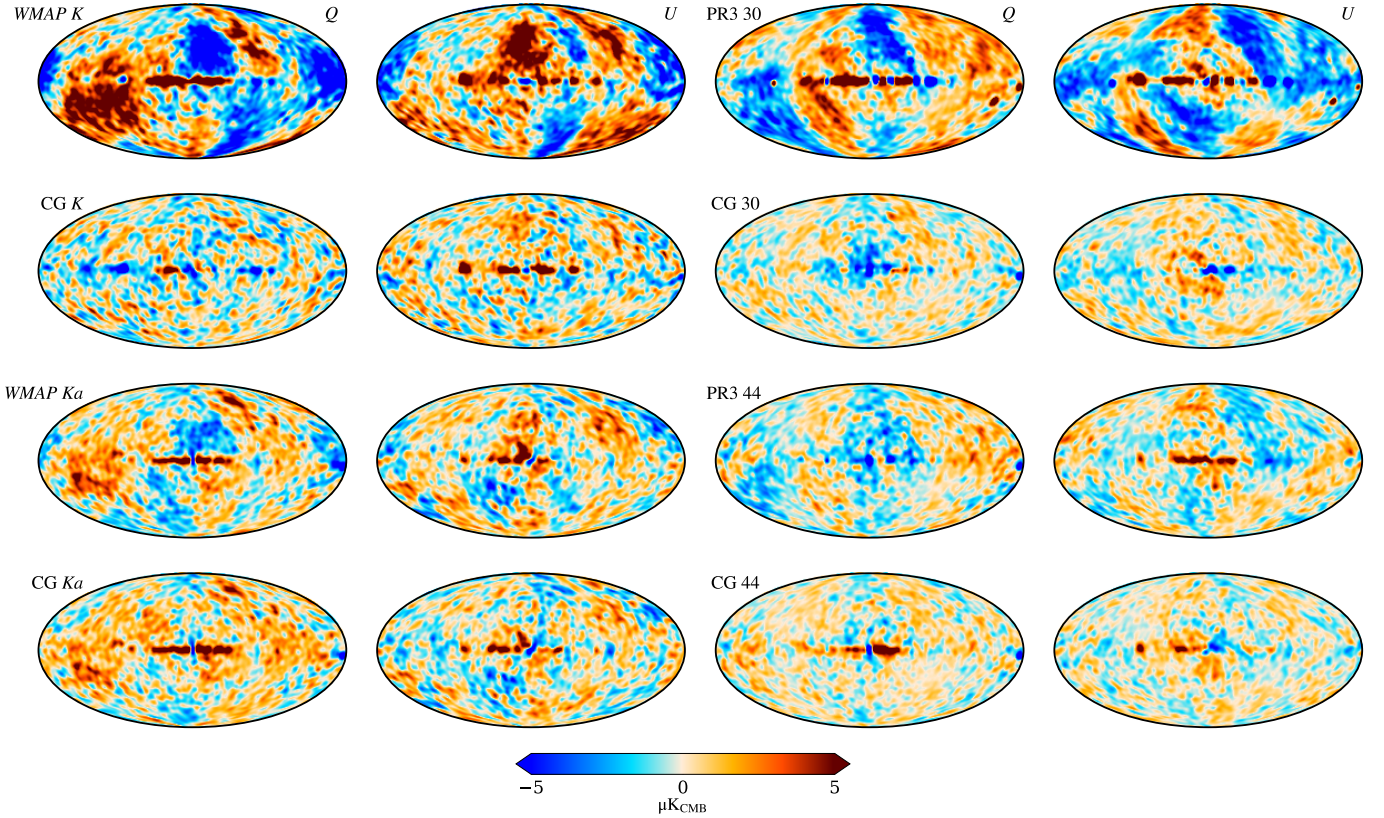


Fig. 3. Residuals with respect to the COSMOGLOBE DR1 sky model evaluated at 5° . Each of the WMAP9, Planck PR3, and COSMOGLOBE maps have had the COSMOGLOBE DR1 sky model evaluated at their respective bandpass and resolution subtracted. COSMOGLOBE maps are labeled CG, Planck 2018 maps are labeled PR3, and the legacy WMAP9 maps are labeled WMAP.

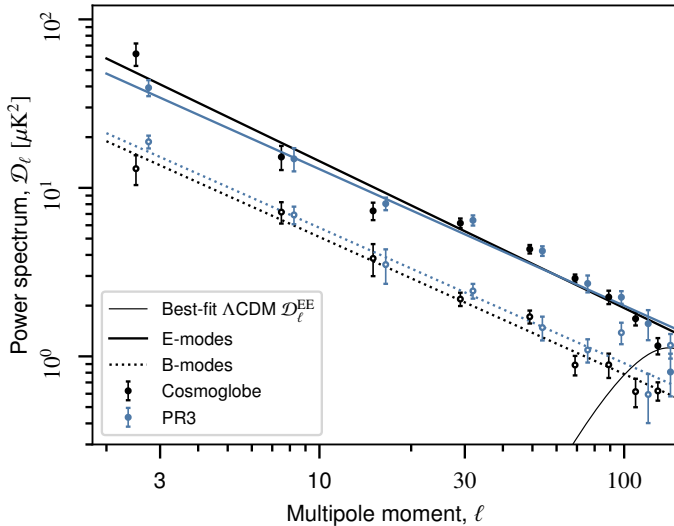


Fig. 4. Half-mission splits of synchrotron for Planck PR3 (black) and COSMOGLOBE DR1 (blue). Filled circles correspond to E -modes, while empty circles correspond to B -modes. The thick solid and dashed lines are the best-fit E - and B -mode power law fits to synchrotron, and the thin black line is the ΛCDM prediction for E -modes.

4. Polarized synchrotron spectral indices

The determination of polarized synchrotron spectral index variation across the sky has been studied in detail using several different data combinations. Although the small-scale details vary,

Table 1. Best-fit power law parameters to the synchrotron estimates evaluated at 30 GHz, using half-mission splits with NaMaster.

	PR3	COSMOGLOBE
$A_{\delta}^{\text{EE}} [\mu\text{K}^2]$...	2.39 ± 0.07	2.35 ± 0.05
$A_{\delta}^{\text{BB}} [\mu\text{K}^2]$...	1.09 ± 0.06	0.94 ± 0.04
$A_{\delta}^{\text{BB}} / A_{\delta}^{\text{EE}}$...	0.46 ± 0.03	0.40 ± 0.02
a_{δ}^{EE}	-0.81 ± 0.02	-0.87 ± 0.02
a_{δ}^{BB}	-0.80 ± 0.03	-0.81 ± 0.03

nearly every analysis has found $\beta_s \simeq 2.8$ in the Galactic plane and $\beta_s \sim -3.3$ in high Galactic latitudes (Fuskeland et al. 2014; Krachmalnicoff et al. 2018; Fuskeland et al. 2021; Weiland et al. 2022), with the exception of QUIJOTE (Rubíñ Martín et al. 2023; de la Hoz et al. 2023), who find a slightly flatter spectral index along the Galactic plane. Both Fuskeland et al. (2014) and Weiland et al. (2022) report oscillations with Galactic longitude close to the Galactic plane, but high-latitude regions variations are more difficult to determine, and tend to depend on the specific dataset chosen and the analysis method chosen.

A fundamental challenge in spectral index estimation is due to the fact that every difference between two channels can be associated with a spectral index variation if not accounted for fully. Therefore, it is necessary to not only make sure that results are robust towards data selection, but also to ensure that differences between results are not due to instrumental effects.

While the COSMOGLOBE pipeline produces samples of polarized synchrotron emission, the spatial variation of the spectral

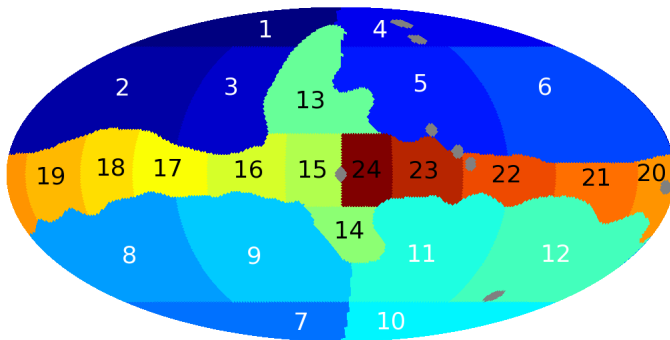


Fig. 5. Spectral index regions as defined in Fuskeland et al. (2014). The most prominent point sources are masked out and shown in grey circular areas.

index is poorly determined within the Gibbs chain. To mitigate the poor Monte Carlo Markov Chain (MCMC) convergence of the spectral indices, the COSMOGLOBE DR1 sampled the spectral index from a prior distribution, $\beta_s \sim \mathcal{N}(-3.15, 0.05)$. Improvements within the Commander3 framework will require more high signal-to-noise data.

In order to test for and mitigate potential instrumental effects, we perform two analyses, a temperature-temperature (T-T) plot analysis in Sect. 4.1 and a Gibbs sampling analysis using Commander1 in Sect. 4.2. Section 4.1 focuses on pairs of channels to better isolate potential unmodeled systematic effects, while Sect. 4.2 uses all WMAP and LFI channels plus *Planck* 353 GHz to maximize the joint statistical weight of all available data.

4.1. T-T plot analysis

The T-T plot analysis can be used for pairs of datasets in a model-independent way, allowing for us to probe the difference between different datasets without making strong assumptions on the underlying physical model. This method can also easily be adapted to probe the dependence on polarization angle. This can be used to determine both the orientation dependence of β_s , as well as identify the magnitude of unmodeled instrumental effects, such as beam asymmetries, as discussed in Wehus et al. (2013).

4.1.1. Method

Following Fuskeland et al. (2014) and Fuskeland et al. (2021), we apply linear regression via the T-T plot method, in which spectral indices can be estimated over extended regions with approximately constant spectral indices. Here we use the regions labeled in Fig. 5. In this approach, our data model for two frequencies is

$$\mathbf{m}_\nu = \mathbf{m}_{\nu_0} \left(\frac{\nu}{\nu_0} \right)^\beta + c_\nu + \mathbf{n}_\nu, \quad (1)$$

where \mathbf{m}_ν is a spatially varying amplitude map at frequency ν , ν_0 is the reference frequency, β the power law between the two frequencies, c_ν the spatially constant offset per band, and \mathbf{n}_ν the noise. In the case of noiseless data with no offset, the spectral index may be estimated using a simple ratio,

$$\frac{m_{\nu_1,p}}{m_{\nu_2,p}} = \left(\frac{\nu_1}{\nu_2} \right)^{\beta_{s,p}} \Rightarrow \beta_{s,p} = \frac{\ln(m_{\nu_1,p}/m_{\nu_2,p})}{\ln(\nu_1/\nu_2)}. \quad (2)$$

In the case where one map is much noisier than the other, the standard T-T plot method involves performing a linear regression

$\mathbf{m}_{\nu_1} = a\mathbf{m}_{\nu_2} + b$, and associates β_s with $\ln a / \ln(\nu_1/\nu_2)$. More care must be taken when the noise amplitudes in both maps are comparable to each other, so we adopt the effective variance method of Orear (1982) as implemented by Fuskeland et al. (2014).

For the T-T plot analysis, we focus exclusively on bands between 23 and 33 GHz. As in Fuskeland et al. (2014), we use the WMAP K and Ka band Stokes Q and U parameter maps at 23 GHz and 33 GHz. The respective effective frequencies used are 22.45 GHz and 32.64 GHz. The maps originally at a HEALPix⁷ pixelization of $N_{\text{side}} = 512$ are downgraded to $N_{\text{side}} = 64$ and smoothed to a common resolution of 1° FWHM. The *Planck* data products used are the 30 GHz Stokes Q and U maps, with an effective frequency of 28.4 GHz. Both the BEYONDPLANCK and COSMOGLOBE products are natively at $N_{\text{side}} = 512$, while for the *Planck* PR4, it is 1024.

As in Fuskeland et al. (2021), a systematic uncertainty that takes into account the variation of β over rotation angle, $[\max(\beta_\alpha) - \min(\beta_\alpha)]/2$, is added in quadrature to the statistical uncertainty. The uncertainty of the spectral indices is calculated as the minimum of the uncertainties in each rotation angle and region. For the COSMOGLOBE analyses we have a whole suite of maps represented by the individual samples instead of just one mean map. Here the standard deviation of the spectral indices of the samples is also added in quadrature to represent an additional systematic uncertainty. This enables us to have a better propagation of uncertainties from the maps to the final spectral indices.

4.1.2. Results

We start by looking at the results from the T-T plot method applied to the K -band and 30 GHz maps. We apply the method to the 24 regions to see the spatial variation of the polarized synchrotron spectral index. The top three maps in Fig. 6 show the T-T plot results using WMAP9 K -band and three incarnations of the *Planck* 30 GHz maps; PR3, PR4, and BEYONDPLANCK. The bottom map shows the results using the improved maps from the COSMOGLOBE analysis, K -band and 30 GHz. The spectral indices are inverse variance weighted over rotation angle, and in the COSMOGLOBE case also over posterior samples. Some of the brightest point sources have been masked out using grey. We see an overall narrowing in the range of spectral spectral indices, from regions with extreme values in the top map represented by dark red and blue values, with colors gradually fading in the lower figures. The range in the plot is quite wide for spectral indices, and goes from -5 to -1 . This improvement in the value of the spectral index is especially prominent in the high Galactic regions, as well as region number 22 along the Galactic plane. Using the COSMOGLOBE DR1 data, we find a full-sky inverse variance weighted mean of the spectral index, $\beta_s = -3.07 \pm 0.07$ while the mean of the high latitude 1–14 is -3.31 ± 0.07 .

The same results are also shown in Fig. 7, with the spectral indices plotted as a function of region number. The different datasets are shown in different colors, and with the same order as the four maps in Fig. 6. Here we have also included one sigma uncertainties as errorbars as described in Sect. 4.1.1. The magnitude of the error bars are set by the reported white noise level in each dataset except for the COSMOGLOBE, which also takes into account systematic uncertainties. We also plot the estimated spectral index range for high Galactic regions, in our case represented by regions 1–12, as forecasted by the likelihood analysis in Figure 22 of Planck Collaboration V (2020). We see with each

⁷ <http://healpix.sourceforge.net>

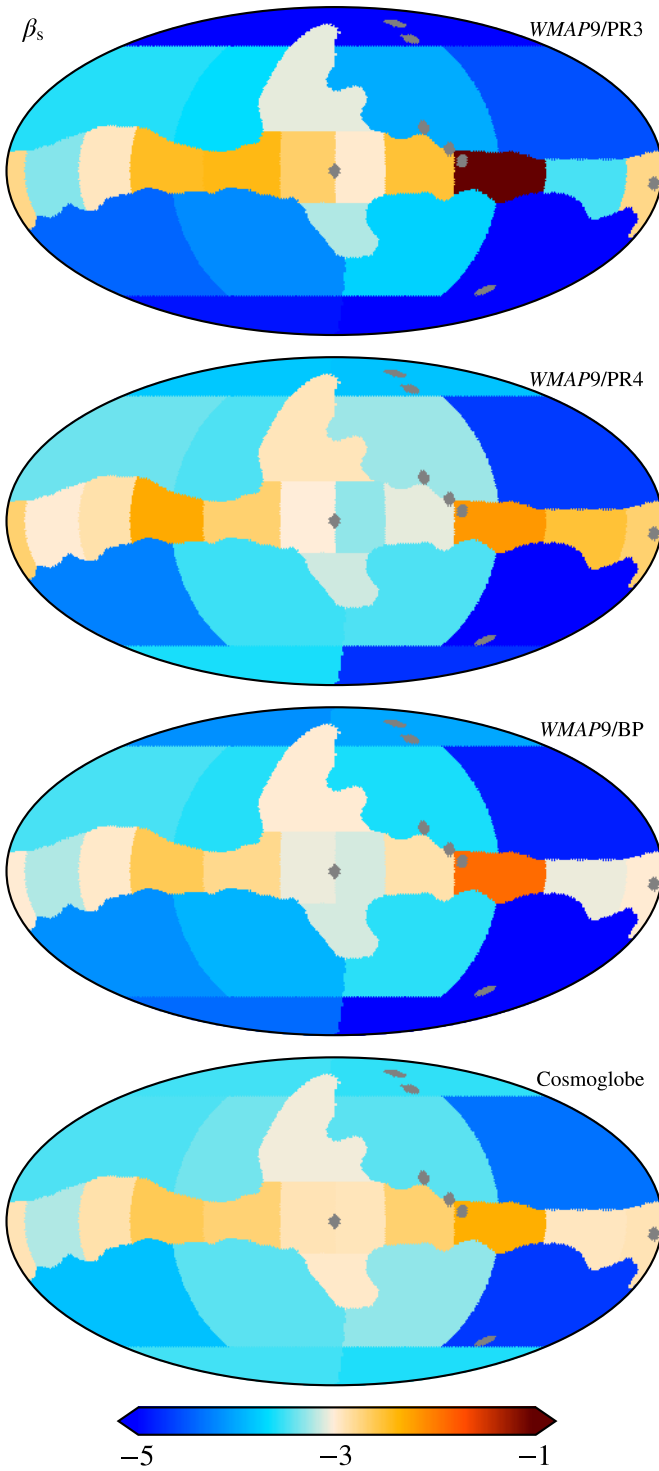


Fig. 6. Spatial variation of the synchrotron spectral index, computed using T-T plot between the (from top to bottom) *WMAP9 K-band and Planck PR3 30 GHz*, *WMAP9 K-band and Planck PR4 30 GHz*, *WMAP9 K-band and BEYONDPLANCK 30 GHz*, and *Cosmoglobe K-band and Cosmoglobe 30 GHz*. The spectral index is inverse variance weighted over rotation angle, and in the *Cosmoglobe* case also samples.

iteration of the data processing, the region estimates draw closer to this line. For a more detailed study of each of the regions, we refer the reader to Appendix A, where we have shown the corresponding T-T scatterplots (Fig. A.1) and the spectral index as a function of rotation angle (Fig. A.2) for all 24 regions.

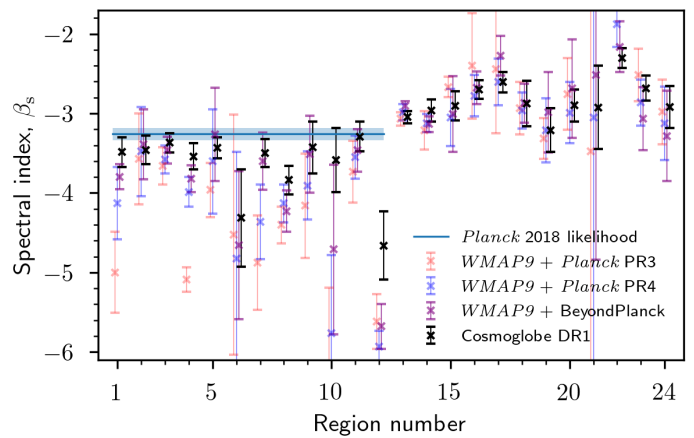


Fig. 7. Synchrotron spectral index as a function of region number, computed using T-T plot between the *WMAP9 K-band and Planck PR3 30 GHz* (red), *WMAP9 K-band and Planck DR4 30 GHz* (blue), *WMAP9 K-band and BEYONDPLANCK 30 GHz* (purple), and *Cosmoglobe K-band and Cosmoglobe 30 GHz* (black). The spectral index is inverse variance weighted over rotation angles, and samples. The horizontal line in the high latitude regions corresponds to the estimated spectral index values from the *Planck 2018* likelihood analysis (Planck Collaboration V 2020).

As a second part of this T-T plot analysis we apply the method on *K*-band and *Ka*-band maps. For the *WMAP* data, this analysis was already performed in Fuskeland et al. (2014), so here we only present results using the new *Cosmoglobe* data. First, as a consistency check, in Fig. 8 we plot the spectral indices for all 24 regions in the form of *Cosmoglobe K/30 GHz* versus *Cosmoglobe K/Ka*. We see that for the regions in the north and south Galactic spurs, and along the Galactic plane (regions 13–24), there is a good agreement between the spectral indices obtained by the two pairs of datasets. Regions 1–12, all of which are high-latitude regions with low signal-to-noise, are all consistent with the two data combinations. The most prominent outliers, regions 6 and 12, are the regions with the lowest signal-to-noise ratio, and hence most prone to unmodeled effects and noise fluctuations.

In Fig. 9 the value of the spectral indices is shown for the 24 regions. We see here that the colors are even fainter than the *Cosmoglobe K-band versus 30 GHz* values (the bottom figure in Fig. 6), meaning there are fewer outliers with respect to a standard value in the range around -3 . This is especially visible in the regions with lowest signal to noise, like regions 6, 8 and 12, at high latitude. Taking the inverse variance weighted mean of the spectral indices of all 24 regions, we get $\beta_s = -2.95 \pm 0.07$, while for the high latitude regions 1–14 we get -3.20 ± 0.10 .

4.2. Parametric component estimation

In this section we use Commander⁸ to perform pixel-based component separation on maps smoothed to a common resolution of 5° and at $N_{\text{side}} = 64$.⁹ For this analysis, we perform 100 pixel-based Commander1 Gibbs samples on each of the 500 *Cosmoglobe* DR1 Gibbs samples produced by Commander3. This allows us to decompose the pure statistical error assuming white noise alone for each of the 100 Commander1 samples, while

⁸ <https://github.com/Cosmoglobe/Commander1>

⁹ We use Commander1 because it is parallelized over pixels and can quickly determine spatial variation, while Commander3 is optimized for multi-resolution data.

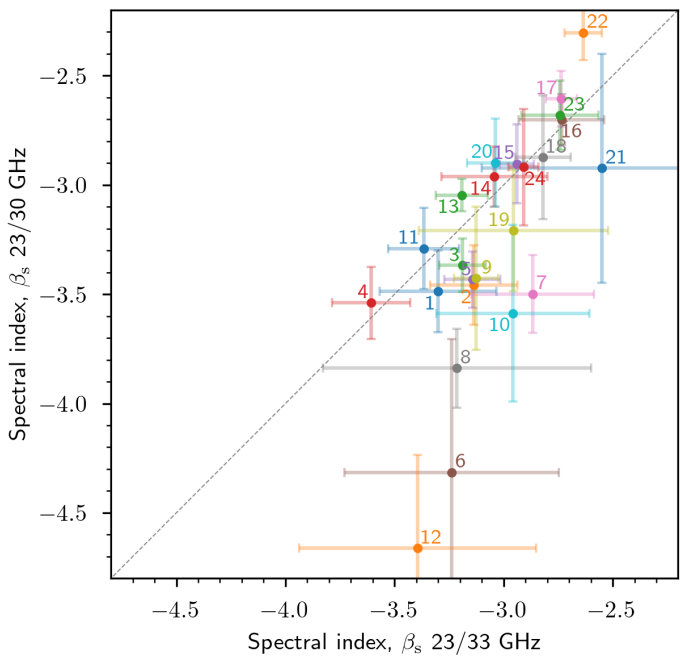


Fig. 8. Synchrotron spectral index computed using T-T plot with the COSMOGLOBE DR1 K -band and 30 GHz data versus COSMOGLOBE DR1 K -band and Ka -band data for the 24 regions.

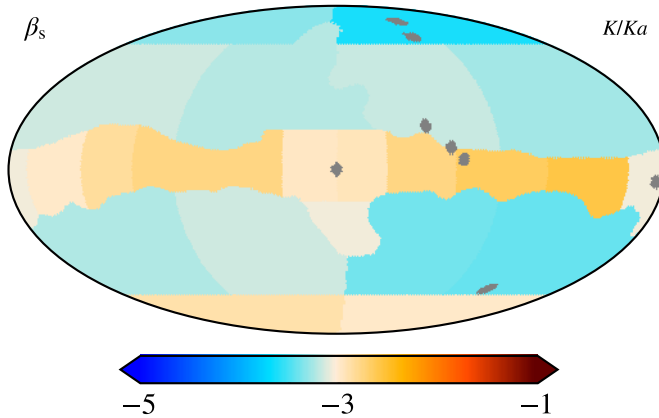


Fig. 9. Spatial variation of the synchrotron spectral index, computed using T-T plot between the COSMOGLOBE DR1 K - and Ka -band. The spectral index is inverse variance weighted over rotation angle and samples.

changes between each main DR1 sample show the effects of low-level instrumental processing. In these analyses, we use the same polarized bands as in the main COSMOGLOBE DR1 analysis, namely *WMAP*, *Planck* LFI, and *Planck* 353 GHz. We use a prior $\beta_s \sim N(-3.1, 0.1)$ for the synchrotron spectral index, while for dust we use a constant spectral index of $\beta_d = 1.55$ and the dust map T_d from [Planck Collaboration X \(2016\)](#).

We used the same data model as in COSMOGLOBE DR1, but allowed for spatially varying β_s in two different forms. First, we allow β_s to vary over the same regions as in the T-T analysis. We find that for such large regions, there is very little effect due to the prior, and in particular find a maximum shift of 0.3 between a prior of $N(-3.5, 0.1)$ and $N(-2.7, 0.1)$. We add this difference in quadrature to the uncertainty due to statistical and systematic errors. We also compare the reported β_s maps from QUIJOTE ([de la Hoz et al. 2023](#)) and CLASS ([Eimer et al. 2023](#)). We choose

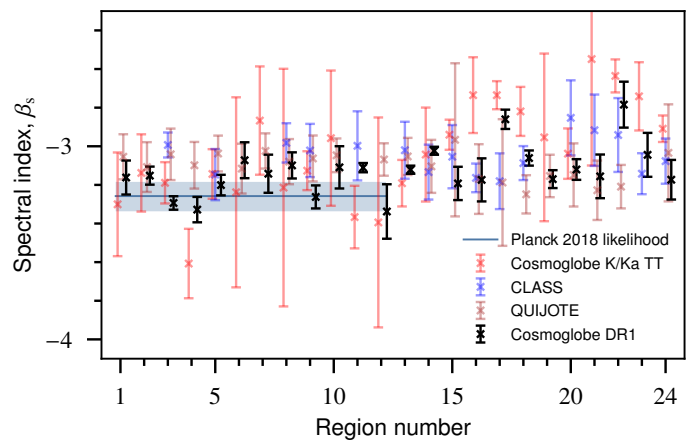


Fig. 10. Spectral index from COSMOGLOBE DR1 spectral index estimation, T-T plots with K/Ka , the QUIJOTE estimates, and the CLASS estimates.

these maps because they are to this date the best publicly available synchrotron spectral index maps that are not affected by Faraday rotation off the Galactic plane, as in S-PASS ([Krachmalnicoff et al. 2018; Fuskeland et al. 2021](#)). The delivered β_s maps are pixelized at $N_{\text{side}} = 64$ and 32, respectively, with associated uncertainty maps taking into account the expected instrumental noise levels. We take an inverse-weighted average of the respective maps and report the weighted standard error within each region, displayed in Fig. 10.

In general, the uncertainties in our analysis are smaller than each of the other published results, each for slightly different reasons. First, the T-T analyses will inherently have less constraining power than a full likelihood analysis, as this approach only uses two frequency channels via a linear regression, so the uncertainty is determined by the noise level in each frequency channel and the inherent variation within a given sky region. Beyond that, the T-T plot in this paper marginalizes over dependence on the polarization angle α , and by design accentuates systematic effects, predominantly beam ellipticity. Finally, the QUIJOTE analysis is most similar in data choice (MFI 11/13 GHz, *WMAP9* K/Ka , *Planck* PR4) and methodology (B-SeCRET; [de la Hoz et al. 2022](#)), but still yields higher uncertainty than the Commander1 spectral index region analysis. This is most likely due to different spatial resolution and modeling choices; the Commander1 analysis presented here is performed at 5° resolution versus the 2° resolution per-pixel analysis in [de la Hoz et al. \(2023\)](#). In addition, [de la Hoz et al. \(2023\)](#) sampled for β_d and T_d with priors $N(1.55, 0.1)$ and $N(21, 3)$ while using a relatively wide prior on β_s of $N(-3.1, 0.3)$.

At high Galactic latitudes (regions 1–12), there is good agreement between each of the treatments, and all values are consistent with a single constant value. In the north and south polar spur (regions 13 and 14) there is excellent agreement between all of the pipelines, while along the Galactic plane (regions 15–24), there are mild discrepancies between the methodologies, in particular a less distinct amount of periodic structure as a function of Galactic latitude.

To more finely probe the spatial variation of β_s , we perform a second Commander1 analysis with identical data and model choices, except the β_s are allowed to vary with a prior of $N(-3.1, 0.1)$ and spatially vary along an $N_{\text{side}} = 16$ grid. We found that this was the highest resolution grid in which the spectral index was not prior dominated across all high-latitude regions. In Fig. 11, we display the mean of all of the Gibbs

samples, along with the standard deviation evaluated per COSMOGLOBE DR1 Gibbs sample, $\sigma_{\beta_s}^{\text{stat}}$, and the standard deviation over all COSMOGLOBE DR1 samples and Commander1 samples, $\sigma_{\beta_s}^{\text{sys+stat}}$. Put concretely, $\sigma_{\beta_s}^{\text{stat}}$ is the standard deviation when the input maps themselves are static, and $\sigma_{\beta_s}^{\text{sys+stat}}$ includes variations in the frequency maps themselves, corresponding to underlying instrumental effects, including gain, noise characterization, and baseline estimation. The uncertainty due to white noise alone traces the high signal-to-noise regions of the polarized synchrotron, especially the prominent loops and spurs and the Fan region. At high Galactic latitudes, the standard deviation is 0.1, indicating that the posterior uncertainty is limited by the prior. To further test this, we performed additional Commander1 runs with priors of $\mathcal{N}(-3.2, 0.1)$ and $\mathcal{N}(-3.0, 0.1)$, and used the deviation from the mean in the fiducial analysis as an estimate of the extent of prior domination, $\sigma_{\beta_s}^{\text{prior}} \equiv (\langle \beta_{-3.0} \rangle - \langle \beta_{-3.2} \rangle)/2$. Adding this in quadrature gives the total uncertainty, which we display in the bottom panel of Fig. 11.

The uncertainty across the entire Gibbs chain does not merely trace high signal-to-noise regions, and in fact there are variations that exceed the prior surrounding the Galactic center. These variations are primarily due to gain and bandpass uncertainties. It therefore makes sense that gain variations in K , Ka , and 30 GHz around the brightest region of the sky would induce large variations. Despite the relative increase in noise level when including instrumental effects, the brightest Galactic loops, the Cygnus region, and Tau A regions are well-constrained by the data. In total, there is not enough high-signal-noise data to credibly claim spatial variation in high Galactic latitude regions.

As a final quality check, we display the residuals with respect to the Commander1 sky model in Fig. 12, as well as the total scaled and normalized χ^2 . In all bands but K , 30 GHz, and Ka , there are no visible artifacts due to instrumental uncertainty, with each map showing fluctuations consistent with the estimated white noise level calculated in the DR1 processing. In addition, many of the residuals visible in Fig. 3 have been reduced, demonstrating that polarized synchrotron spectral index variation provides meaningful improvements to the sky model fit.

The most salient remaining residuals are in K , 30 GHz, and Ka . K -band and 30 GHz are anticorrelated surrounding Galactic center, indicating tension between these two high signal-to-noise datasets. This could either be due to genuine mismodeling of the sky, or be due to incompletely modelled instrumental parameters. In particular, the signature is reminiscent of bandpass leakage corrections, which are shown, e.g., in Fig. 9 of Svalheim et al. (2023b).

A more persistent residual is found in the Stokes Q Ka -band map. This feature has appeared in several different analyses, e.g., Fig. 4 of Svalheim et al. (2023a) and Fig. 8 of Weiland et al. (2022), but was not as clear without full removal of the poorly measured modes in the final map. The lack of this feature in the corresponding Stokes U map suggests that the effect is not a true Galactic effect, and is in some way due to instrumental processing, or unmodeled systematics. We discuss potential sources of this signal in Sec. 5.

5. Discussion and conclusion

We have presented the state-of-the-art model of polarized synchrotron using the COSMOGLOBE DR1 data products. The polarized synchrotron map as delivered in Watts et al. (2023a) has an effective white noise level of $3.4 \mu\text{K}$, a 29 % improvement over

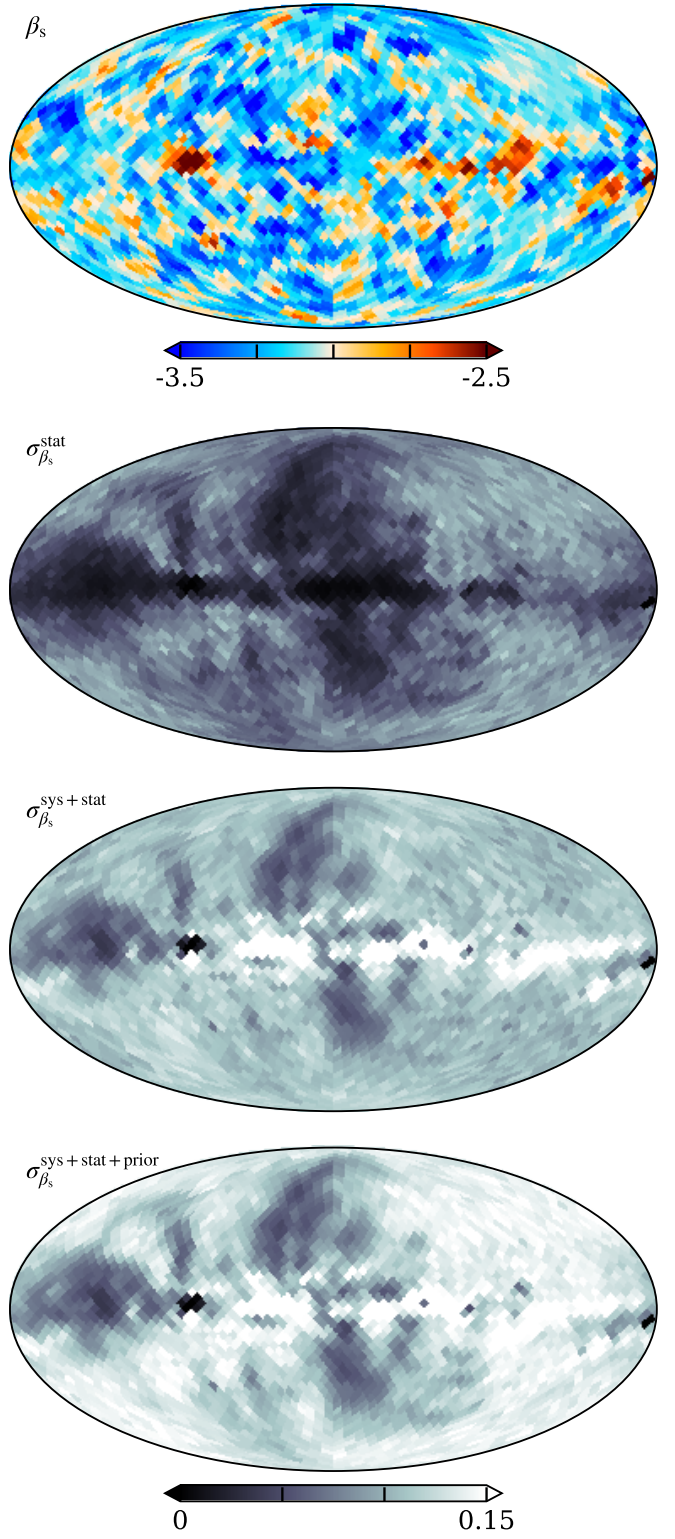


Fig. 11. COSMOGLOBE DR1 β_s constraints. (First): Mean spectral index over all samples, (second): standard deviation over a single COSMOGLOBE DR1 sample, (third): standard deviation over all Commander1 and COSMOGLOBE DR1 samples, and (fourth): difference due to prior choice added in quadrature.



Fig. 12. Residual maps and normalized χ^2 for the Commander1 analysis of the COSMOGLOBE DR1 data. Panels are organized with LFI channels in rows 1–2, WMAP in rows 3–7, and the total reduced χ^2 in row 8.

the white noise levels of the *WMAP* *K*-band and LFI 30 GHz maps. Using the fully consistent reprocessed *WMAP* and *Planck* LFI data, we have been able to leverage the full statistical power of both datasets. We have additionally verified that this model characterizes the polarized sky signal to within 5 μK at all bands. We have also reproduced the previously-reported *E*-to-*B*-mode ratio in the polarized synchrotron power spectrum. Furthermore, we have shown that physically reasonable spectral indices can be recovered using a variety of methods, which are consistent with both the methods presented in this paper and with previously published results from CLASS and QUIJOTE, confirming variation in β_s along the Galactic plane and constant at high Galactic latitudes.

Our improved processing of the *WMAP* and LFI data in conjunction with improved polarized synchrotron modeling has allowed us to dig deeper into the underlying differences between the two datasets. We have shown agreement between the β_s values derived using the T-T plot using *K*/30 GHz and *K*/*Ka* data combinations, further evidence that these datasets are now consistent with each other. The remaining unexplained differences between the sky maps and our derived model are primarily in the Galactic center, and have morphologies consistent with bandpass errors and SED complexities.

The least well-understood residual is in the *Ka*-band, specifically Stokes *Q*. Of all the known instrumental effects in both *WMAP* and *Planck* LFI, the only one that morphologically resembles this residual is the bandpass correction in *K*-band, which was previously presented in Figure 12 of Watts et al. (2023a). The bandpass correction term depends solely on laboratory measurements, presented in Jarosik et al. (2003). The high statistical weight of *K*-band for determining polarized synchrotron could easily lead to an undersubtraction in the *Ka*-band maps. Conversely, the bandpass correction to *Ka*-band itself is negligible, as all of the *Ka*-band radiometers were reported to have nearly identical bandpasses. A full accounting of this effect, including sampling of bandpass differences in the *WMAP* TODs (not performed in Watts et al. 2023a) will be performed in future work.

The estimation of β_s is difficult precisely because the quantity is dependent on differences between different frequencies, which can often exacerbate systematic effects and processing choices. The differences between a sky model and datasets is best determined in the timestreams – much of the improvement demonstrated in this analysis would not have been possible through a purely map-based analysis. Beyond pure improvement of data quality, this approach allowed for a natural end-to-end propagation of errors, and demonstrated that some of the brightest regions of the sky in fact do not have well-determined spectral indices, despite their high signal-to-instrumental noise ratio. As increasingly stringent uncertainty constraints are becoming necessary in order to measure a non-zero tensor-to-scalar ratio, the use of joint information between experiments with complementary observation strategies will increasingly become a necessity. Future joint analysis, including for example QUIJOTE and CLASS data, will continue to improve our knowledge of the polarized sky.

Acknowledgements. We thank the entire *Planck* and *WMAP* teams for invaluable support and discussions, and for their dedicated efforts through several decades without which this work would not be possible. The current work has received funding from the European Union’s Horizon 2020 research and innovation programme under grant agreement numbers 819478 (ERC; COSMOGLOBE) and 772253 (ERC; brs2COSMOLOGY). In addition, the collaboration acknowledges support from RCN (Norway; grant no. 274990). This project has received funding from the European Union’s Horizon 2020 research and innovation programme under the Marie Skłodowska-Curie grant agreement No 101007633.

The research was carried out in part at the Jet Propulsion Laboratory, California Institute of Technology, under a contract with the National Aeronautics and Space Administration (80NM0018D0004). We acknowledge the use of the Legacy Archive for Microwave Background Data Analysis (LAMBDA), part of the High Energy Astrophysics Science Archive Center (HEASARC). HEASARC/LAMBDA is a service of the Astrophysics Science Division at the NASA Goddard Space Flight Center. Some of the results in this paper have been derived using the `healpy` and `HEALPix`¹⁰ packages (Górski et al. 2005; Zonca et al. 2019). This work made use of `Astropy`:¹¹ a community-developed core Python package and an ecosystem of tools and resources for astronomy (Astropy Collaboration et al. 2013, 2018, 2022).

References

- Abazajian, K., Addison, G., Adshead, P., et al. 2019, arXiv e-prints, arXiv:1907.04473
- Ade, P., Aguirre, J., Ahmed, Z., et al. 2019, *J. Cosmology Astropart. Phys.*, 2019, 056
- Ade, P. A. R., Ahmed, Z., Amiri, M., et al. 2021, *Phys. Rev. Lett.*, 127, 151301
- Alonso, D., Sanchez, J., Slosar, A., & LSST Dark Energy Science Collaboration. 2019, *MNRAS*, 484, 4127
- Astropy Collaboration, Price-Whelan, A. M., Lim, P. L., et al. 2022, *ApJ*, 935, 167
- Astropy Collaboration, Price-Whelan, A. M., Sipőcz, B. M., et al. 2018, *AJ*, 156, 123
- Astropy Collaboration, Robitaille, T. P., Tollerud, E. J., et al. 2013, *A&A*, 558, A33
- Basyyrov, A., Suur-Uski, A.-S., Colombo, L. P. L., et al. 2023, *A&A*, 675, A10
- Bennett, C. L., Banday, A. J., Gorski, K. M., et al. 1996, *ApJ*, 464, L1
- Bennett, C. L., Larson, D., Weiland, J. L., et al. 2013, *ApJS*, 208, 20
- BeyondPlanck Collaboration. 2023, *A&A*, 675, A1
- BICEP2/Keck Array and Planck Collaborations. 2015, *Phys. Rev. Lett.*, 114, 101301
- de Belsunce, R., Gratton, S., & Efstathiou, G. 2022, *MNRAS*, 517, 2855
- de la Hoz, E., Barreiro, R. B., Vielva, P., et al. 2023, *MNRAS*, 519, 3504
- de la Hoz, E., Diego-Palazuelos, P., Martínez-González, E., et al. 2022, *J. Cosmology Astropart. Phys.*, 2022, 032
- Delabrouille, J., Betoule, M., Melin, J.-B., et al. 2013, *A&A*, 553, A96
- Eimer, J. R., Li, Y., Brewer, M. K., et al. 2023, arXiv e-prints, arXiv:2309.00675
- Fuskeland, U., Andersen, K. J., Aurlien, R., et al. 2021, *A&A*, 646, A69
- Fuskeland, U., Wehus, I. K., Eriksen, H. K., & Næss, S. K. 2014, *ApJ*, 790, 104
- Galloway, M., Andersen, K. J., Aurlien, R., et al. 2023, *A&A*, 675, A3
- Górski, K. M., Hivon, E., Banday, A. J., et al. 2005, *ApJ*, 622, 759
- Haslam, C. G. T., Salter, C. J., Stoffel, H., & Wilson, W. E. 1982, *A&AS*, 47, 1
- Hauser, M. G., Arendt, R. G., Kelsall, T., et al. 1998, *ApJ*, 508, 25
- Jarosik, N., Barnes, C., Greason, M. R., et al. 2007, *ApJS*, 170, 263
- Jarosik, N., Bennett, C. L., Halpern, M., et al. 2003, *ApJS*, 145, 413
- Kandel, D., Lazarian, A., & Pogosyan, D. 2017, *MNRAS*, 472, L10
- Krachmalnicoff, N., Carretti, E., Baccigalupi, C., et al. 2018, *A&A*, 618, A166
- LiteBIRD Collaboration, Ally, E., Arnold, K., et al. 2023, *Progress of Theoretical and Experimental Physics*, 2023, 04F021
- Madhavacheril, M. S., Qu, F. J., Sherwin, B. D., et al. 2023, arXiv e-prints, arXiv:2304.05203
- Mather, J. C., Cheng, E. S., Cottingham, D. A., et al. 1994, *ApJ*, 420, 439
- Neronov, A., Malyshev, D., & Semikoz, D. V. 2017, *A&A*, 606, A22
- Orear, J. 1982, *American Journal of Physics*, 50, 912
- Orlando, E. & Strong, A. 2013, *MNRAS*, 436, 2127
- Page, L., Hinshaw, G., Komatsu, E., et al. 2007, *ApJS*, 170, 335
- Planck Collaboration X. 2016, *A&A*, 594, A10
- Planck Collaboration I. 2020, *A&A*, 641, A1
- Planck Collaboration II. 2020, *A&A*, 641, A2
- Planck Collaboration IV. 2018, *A&A*, 641, A4
- Planck Collaboration V. 2020, *A&A*, 641, A5
- Planck Collaboration Int. LVII. 2020, *A&A*, 643, A42
- Rubiño-Martín, J. A., Guidi, F., Génova-Santos, R. T., et al. 2023, *MNRAS*, 519, 3383
- Rybicki, G. B. & Lightman, A. P. 1985, *Radiative Processes in Astrophysics* (New York, NY: Wiley)
- Smoot, G. F., Bennett, C. L., Kogut, A., et al. 1992, *ApJ*, 396, L1
- SPIDER Collaboration, Ade, P. A. R., Amiri, M., et al. 2022, *ApJ*, 927, 174
- Svalheim, T. L., Andersen, K. J., Aurlien, R., et al. 2023a, *A&A*, 675, A14
- Svalheim, T. L., Zonca, A., Andersen, K. J., et al. 2023b, *A&A*, 675, A9
- Thorne, B., Dunkley, J., Alonso, D., & Næss, S. 2017, *MNRAS*, 469, 2821
- Vacher, L., Aumont, J., Boulanger, F., et al. 2023, *A&A*, 672, A146
- Watts, D. J., Basyyrov, A., Eskilt, J. R., et al. 2023a, arXiv e-prints, arXiv:2303.08095
- Watts, D. J., Galloway, M., Ihle, H. T., et al. 2023b, *A&A*, 675, A16
- Wehus, I. K., Fuskeland, U., & Eriksen, H. K. 2013, *ApJ*, 763, 138
- Weiland, J. L., Addison, G. E., Bennett, C. L., Halpern, M., & Hinshaw, G. 2022, *ApJ*, 936, 24
- Weiland, J. L., Osumi, K., Addison, G. E., et al. 2018, *ApJ*, 863, 161
- Zonca, A., Singer, L., Lenz, D., et al. 2019, *Journal of Open Source Software*, 4, 1298
- Zonca, A., Thorne, B., Krachmalnicoff, N., & Borrill, J. 2021, *Journal of Open Source Software*, 6, 3783

¹⁰ <http://healpix.sf.net>

¹¹ <http://www.astropy.org>

Appendix A: T-T Plots

This section shows two intermediate results in the T-T plot analysis. Figure A.1 shows the scatter plots within each individual region for both the *WMAP9* and COSMOGLOBE DR1 results, while Fig. A.2 shows the measured spectral index as a function of polarization angle α . For more details, the interested reader can consult [Fuskeland et al. \(2014\)](#).



Fig. A.1. T-T plots for Stokes Q and U maps of the COSMOGLOBE DR1 K -band versus the COSMOGLOBE DR1 30 GHz (black) and the *WMAP9* K -band versus *Planck* PR3 30 GHz (red) for all regions. The horizontal (solid and dotted) lines indicate the corresponding inverse variance weighted values of the spectral index, averaged over rotation angle, and in the COSMOGLOBE case also weighted over samples.



Fig. A.2. Synchrotron spectral index as a function of rotation angle, computed using T-T plot between the COSMOGLOBE DR1 K -band and the COSMOGLOBE DR1 30 GHz (black) compared to the spectral index using the WMAP9 K -band and *Planck* PR3 30 GHz (red) for all regions. The horizontal (solid and dotted) lines indicates the corresponding inverse variance weighted values of the spectral index, averaged over rotation angle, and in the COSMOGLOBE case also samples.